VIP **Gas-Phase Chemistry** *Very Important Paper*

Gas-Phase Mechanism of O•−/Ni2+-Mediated Methane Conversion to Formaldehyde

Ya-Ke Li, Fabian Müller, Wieland Schöllkopf, Knut R. Asmis,* and Joachim Sauer*

Abstract: The gas-phase reaction of $NiAl_2O_4^+$ with CH_4 is studied by mass spectrometry in combination with vibrational action spectroscopy and density functional theory (DFT). Two product ions, $NiAl_2O_4H^+$ and $NiAl_2O_3H_2^+$, are identified in the mass spectra. The DFT calculations predict that the global minimum-energy isomer of $NiAl_2O_4^+$ contains Ni in the $+II$ oxidation state and features a terminal Al–O•− oxygen radical site. They show that methane can react along two competing pathways leading to formation of either a methyl radical ($CH_3^•$) or formaldehyde (CH_2O). Both reactions are initiated by hydrogen atom transfer from methane to the terminal $O^{•−}$ site, followed by either $CH_3^•$ loss or $CH_3^•$ migration to an $O^{2−}$ site next to the Ni^{2+} center. The $CH_3^•$ attaches as CH_3^+ to $O^{2−}$ and its unpaired electron is transferred to the Ni-center reducing it to Ni^+. The proposed mechanism is experimentally confirmed by vibrational spectroscopy of the reactant and two different product ions.

There is a growing interest in tailoring the properties of pristine and doped aluminas as well as alumina-supported transition metal oxides, because of their widespread use in heterogeneous catalysis, in general, and for C–H bond activation, in particular.[1] A promising approach is the

doping of alumina with 3d transition metal ions, since those ions can act as redox-active catalytic centers allowing for more efficient conversions. Moreover, most transition metals of interest are largely available and mostly non-toxic, in contrast to noble metal catalysts that are currently used. Nickel ions, for example, were recently shown to be particularly successful in activating C–H bonds of alkanes and alkenes.[2]

In order to improve the performance of existing materials and to rationally design new single-site catalysts,[3] studies on gas-phase clusters have proven quite helpful. Clusters serve as models for a catalyst's isolated active site.[4] They can be studied under isolated and well-defined conditions and, in combination with quantum chemical calculations, allow researchers to uncover reaction mechanisms operative at the molecular level.[5]

Since methane is the simplest hydrocarbon and at the same time economically highly relevant, it is often used as prototypical substrate for studying the basic reactivity of heteronuclear metal oxide clusters.[6] Recently, metal-doped aluminum oxide ions, such as the $MAl_2O_4^+$ model systems shown in Figure 1, have attracted considerable attention.[6g,n] Whereas $Al_3O_4^+$ (M=Al) exhibits a cone-like geometric structure[7] with a closed-shell electronic structure and is unreactive towards methane, substitution with a transition metal (TM) ion, e.g. Fe^{3+}, results in $Fe^{3+}(d^5)/O^{2−} \leftrightarrow Fe^{2+}(d^6)/O^{•−}$ valence isomerism accompanied by structural rearrange-

[*]   Dr. Y.-K. Li, Dr. F. Müller, Prof. Dr. K. R. Asmis
Wilhelm-Ostwald Institut für Physikalische und Theoretische Chemie, Universität Leipzig
Linnéstr. 2, 04103 Leipzig (Germany)
E-mail: knut.asmis@uni-leipzig.de

Dr. Y.-K. Li, Dr. F. Müller, Dr. W. Schöllkopf
Fritz-Haber-Institut der Max-Planck-Gesellschaft
Faradayweg 4–6, 14195 Berlin (Germany)

Dr. F. Müller, Prof. Dr. J. Sauer
Institut für Chemie, Humboldt-Universität zu Berlin
Unter den Linden 6, 10099 Berlin (Germany)
E-mail: js@chemie.hu-berlin.de

Dr. Y.-K. Li
Present address: Green Catalysis Center and College of Chemistry, Zhengzhou University
Zhengzhou 450001 (China)
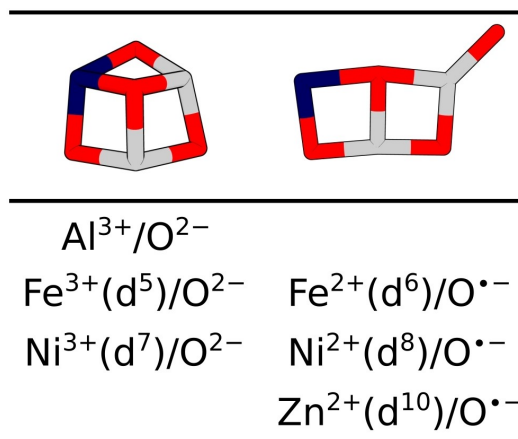
Figure 1. The two most relevant $MAl_2O_4^+$ isomers (aluminum: gray, oxygen: red) and their respective electron configurations for M=Al, Fe, Ni and Zn. While in the tricyclic cone-like structure (left) the metal site M^{3+} (dark blue) is found to be trivalent, it is reduced to M^{2+} in the ladder-like isomer (right) resulting in a terminal oxygen radical.

ment with formation of a highly reactive terminal oxygen radical anion (Figure 1).[6n] Both $FeAl_2O_4^+$ [6n] and $ZnAl_2O_4^+$ [6g] have been found to abstract hydrogen from methane under formation of a methyl radical.

$$CH_3-H + TM^{m+}(d^n)/O^{\bullet-} \rightarrow CH_3^{\bullet} + TM^{m+}(d^n)/HO^- \quad (1)$$
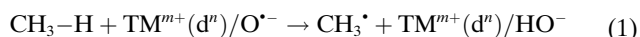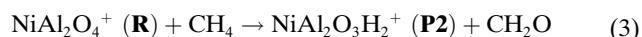
The question thus arises, how these insights can be generalized to other TM ions.

Here, we investigate the reactivity of $MAl_2O_4^+$ with M=Ni towards methane and demonstrate that it is characteristically different from the systems with M=Fe, Zn. Typically, reactivity studies involving gas-phase clusters rely solely on the combination of mass spectrometry with quantum chemical calculations, the vast majority of them using density functional theory (DFT).[8] Consequently, the relevant structures are not experimentally verified, which is problematic, since DFT alone is not predictive, in particular when partially filled d-shells of transition metal ions are involved.[6n] Therefore, in addition to the mass spectrometric investigation of the $NiAl_2O_4^+ + CH_4$ reaction, we use cryogenic ion trap vibrational spectroscopy[9] to determine both the reactant and product ion structures predicted by DFT. Based on these experimentally confirmed structures we propose a reaction mechanism that involves a terminal oxygen-centered radical anion separated from a redox active Ni^{2+} center and that rationalizes why $NiAl_2O_4^+$ activates methane yielding both formaldehyde and a methyl radical.

$NiAl_2O_4^+$ is formed by laser ablation and its reactivity towards CH_4 is studied in a temperature-controllable ion trap reactor under multiple-collision conditions at 100 and 300 K. Figure 2a shows the reference mass spectrum at

100 K obtained after trapping of $NiAl_2O_4^+$ in pure He (5 Pa) for 200 ms (see Figure S1 for He tagging at 10 K). As expected, only the parent ion is observed in the absence of methane. Figures 2b and c show the corresponding ion distribution for a $\approx 0.01\%$ methane in He gas mix (5 Pa) at 100 and 300 K, respectively. Two reaction channels are observed which we assign, based on DFT calculations (see below), to methyl radical or formaldehyde formation:
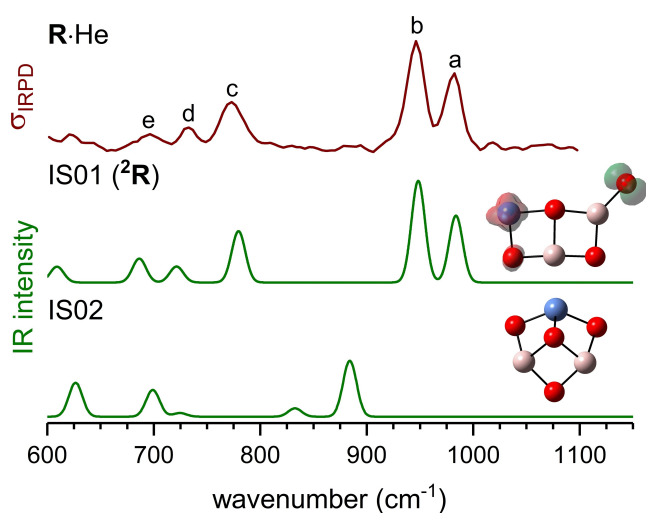
$$NiAl_2O_4^+ (\mathbf{R}) + CH_4 \rightarrow NiAl_2O_4H^+ (\mathbf{P1}) + CH_3^{\bullet} \quad (2)$$

$$NiAl_2O_4^+ (\mathbf{R}) + CH_4 \rightarrow NiAl_2O_3H_2^+ (\mathbf{P2}) + CH_2O \quad (3)$$

The additional mass peaks observed in Figures 2b and c at mass-to-charge ratios m/z of 177, 162, 193 and 178 correspond to $NiAl_2O_4H^+$ (**P1**), $NiAl_2O_3H_2^+$ (**P2**) as well as their complexes with methane, respectively. Those peaks are absent for the reaction of undoped $Al_3O_4^+$ with CH_4 (Figure S3). Formation of weakly bound complexes with methane is favoured at lower temperatures and higher methane partial pressures. Increasing the ion-trap temperature to 300 K i) removes these weakly bound methane complexes from the mass spectrum and ii) enhances the formation of complexes with H_2O, which is a common impurity in mass spectrometers at room temperature. The assignment is further confirmed by isotopic labelling experiments with CD_4 (Figure 2d). The **P1** ($+CH_3^{\bullet}$) and **P2** ($+CH_2O$) formation efficiencies (both including CH_4 adsorption complexes) expectedly depend on temperature and methane partial pressure. In more detail, the **P1/P2** yield ratio increases from 2.3 to 3.8 (with $\pm 20\%$ error) when increasing the ion trap temperature from 100 to 300 K.

Mass spectrometry typically only yields information on the mass-to-charge ratios, but little structural information. In order to characterize the geometric structure of the relevant ions, we therefore performed IRPD spectroscopy on **R**, **P1** and **P2**. Here, the formation of the corresponding weakly bound methane complexes (cf. Figures 2 and S2) comes in handy, since these allow measuring IRPD spectra in the linear absorption regime, i.e. the IRPD cross section is typically directly proportional to the relative intensities in the computed spectra derived from a harmonic frequency analysis.[10]

Figure 3 compares the experimental IRPD spectrum of He-tagged $NiAl_2O_4^+$ (**R**·He) at 10 K with the harmonic IR spectra of the two most stable isomers predicted by DFT (B3P86 functional[11]/TZVP basis sets[12]), labelled IS01 and IS02. It is obvious that the spectrum predicted for IS01 shows much better agreement than the one predicted for IS02. This is also reflected in the values of 0.91 (IS01) and 0.31 (IS02) for the cosine similarity score S, which provides a quantitative measure for the agreement between experimental and theoretical spectra. The score can vary from zero to one, with a value closer to one indicating greater similarity.[13] This comparison unambiguously confirms that $NiAl_2O_4^+$, like $FeAl_2O_4^+$, prefers a planar ladder-like C_s structure containing a terminal oxygen-centred radical anion over the cone-like structure observed for $Al_3O_4^+$.[7]
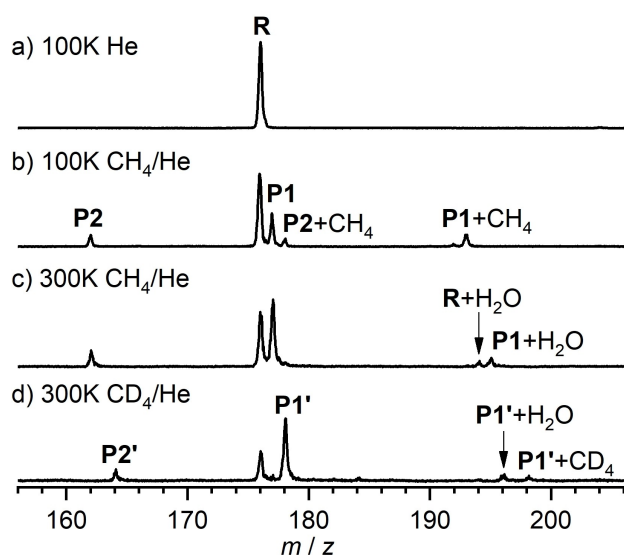
Figure 2. Time-of-flight mass spectra obtained after storing mass-selected $^{58}NiAl_2O_4^+$ ions up to 200 ms in the ion trap filled with a) He at 100 K, b),c) $\approx 0.01\%$ CH_4 in He at 100 K (b) and 300 K (c), and d) $\approx 0.03\%$ CD_4 in He at 300 K. The reactant ion $NiAl_2O_4^+$ is labelled as **R**, the product ions $NiAl_2O_4H^+$ and $NiAl_2O_3H_2^+$ are indicated as **P1** and **P2**, respectively. The deuterium-labelled product ions $NiAl_2O_4D^+$ and $NiAl_2O_3D_2^+$ are indicated as **P1′** and **P2′**, respectively.

Angew. Chem. Int. Ed. **2022**, 61, e202202297 (2 of 6)

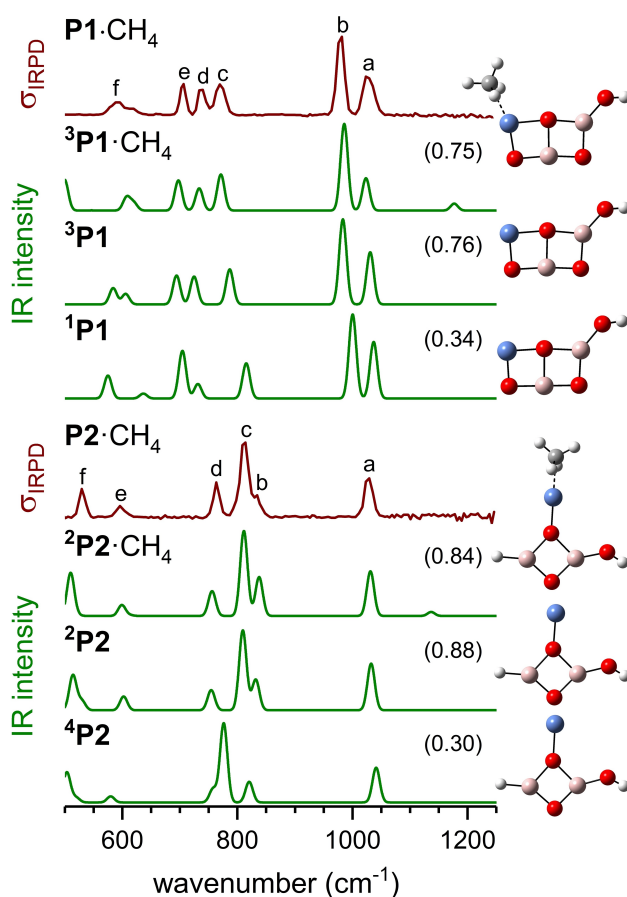© 2022 The Authors. Angewandte Chemie International Edition published by Wiley-VCH GmbH

Figure 3. Experimental IRPD spectrum (dark red) of helium-tagged NiAl$_2$O$_4$$^+$ (**R**·He). See Table S1 for positions and assignments of peaks a–e. Unscaled harmonic DFT (B3P86/TZVP) IR spectra (green), convolved using a Gaussian line shape function with a full-width-at-half-maximum of 15 cm^{-1}, and minimum-energy structures (blue, Ni; pink, Al; red, O) of the two lowest energy isomers IS01 (**^{2}R**) and IS02 of NiAl$_2$O$_4$$^+$ in its doublet state (see Figure S4 for additional information on low energy isomers). For the IS01 (**^{2}R**) structure, the spin distribution is shown; green indicates β-electron excess, red indicates α-electron excess.

For the ground state of the reactant ion **R**, two quasi-degenerate spin states (see Figures S4,S5) are found, a doublet **^{2}R** (IS01) and a quartet **^{4}R** (IS07), which result from the parallel and antiparallel orientation of the spin at the terminal oxygen radical and the spin of the two unpaired electrons of the Ni^{2+}(d^8) ion. The two states differ by 0.3 kJ mol^{-1} in energy (B3P86/TZVP) and have virtually identical structures and harmonic IR spectra. The situation is comparable to FeAl$_2$O$_4$$^+$.[6n]

After identifying the structure of the reactant ion **R**, we performed a comprehensive study of the low-lying minimum-energy structures of the two product ions, NiAl$_2$O$_4$H$^+$ (**P1**) and NiAl$_2$O$_3$H$_2$$^+$ (**P2**). The results are summarized in Figure S6, see Figures S7 and S9 for a comparison of the corresponding harmonic IR spectra of these isomers to the IRPD spectra of CH$_4$-tagged **P1** and **P2**. The influence of the tagging site on the IR spectrum was also considered (see Figures S8 and S10) and found to be negligible. Figure 4 summarizes all results (see Table S1 for peak positions and assignments). The structures of **P1** and **P2** can be unambiguously assigned to the corresponding spin states **^{3}P1** (IS01) and **^{2}P2** (IS07), respectively. The spectra of the corresponding isomers with alternative spin multiplicity (**^{1}P1**, **^{4}P2**) result in significantly lower S values.

To rationalize the formation of **P1** and **P2**, we explored the potential energy surface (PES) of the NiAl$_2$O$_4$$^+$ + CH$_4$ reaction. Figure 5 shows the lowest energy intermediates and transition structures. Methane is activated by the terminal oxygen radical site of **^{2}R**, forming a stable intermediate with an O–H bond and a weakly coordinated $^\bullet$CH$_3$ radical:


Figure 4. Comparison of the experimental IRPD spectra (dark red) of the two methane-tagged product ions NiAl$_2$O$_4$H$^+$ (**P1**·CH$_4$) and NiAl$_2$O$_3$H$_2$$^+$ (**P2**·CH$_4$) at 100 K to the unscaled harmonic DFT(B3P86/TZVP) spectra (green) of triplet **^{3}P1**·CH$_4$, triplet **^{3}P1**, and singlet **^{1}P1** (upper panels), as well as doublet **^{2}P2**·CH$_4$, doublet **^{2}P2**, and quartet **^{4}P2** (lower panels), respectively. The harmonic spectra were convolved with a Gaussian line shape function with a full-width-at-half-maximum of 15 cm^{-1}. The cosine similarity score S is given in parentheses and the minimum-energy structure is shown on the right (blue, Ni; pink, Al; red, O; grey, C; white, H). See Table S1 for peak assignments.

$$CH_3-H + [Ni^{2+}(d^8),O^{\bullet-}] \rightarrow CH_3^\bullet + [Ni^{2+}(d^8),HO^-] \quad (4)$$

This hydrogen atom transfer (HAT) step does not necessarily require the formation of an encounter complex (**^{2}1c**→**^{2}1c**/**^{2}2c**→**^{2}2c**, Figure S13) but can also proceed without a barrier (**^{2}R**→**^{2}1**, Figure 5). Both pathways eventually join in the intermediate **^{2}2**, after overcoming a small barrier of 10 and 6 kJ mol^{-1}, respectively. The methyl radical can move from the Al-OH moiety in **^{2}2** to the second, central Al site, **^{2}3**, where it is marginally more stable. The product **^{3}P1** (NiAl$_2$O$_4$H$^+$) + $^\bullet$CH$_3$ can be formed from intermediates **^{2}1**, **^{2}2** or **^{2}3**. Note that dissociation of $^\bullet$CH$_3$ is always entropically favored (vide infra).

Besides adsorption at an Al site, the methane molecule can also attach to the Ni atom which leads to the most stable encounter complex (Figure S13). However, C–H bond activation of methane attached to the Ni-site features, without exception, barriers that are higher in energy than
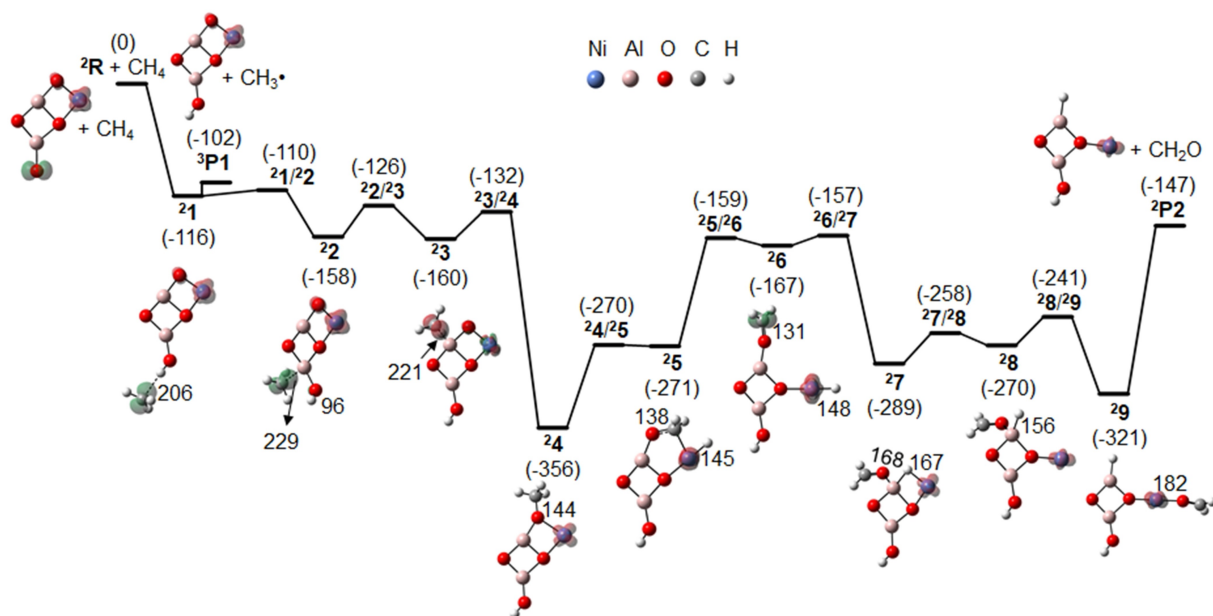
Figure 5. Energy profile for the reaction of $NiAl_2O_4^+$ (doublet) with CH_4 calculated with DFT (B3P86/TZVP). The relative enthalpies at 0 K (equal to the sum of electronic and zero-point vibrational energies), ΔH_0, are given in $kJ\,mol^{-1}$ and bond lengths are given in pm. Along with the minimum-energy structures (blue, Ni; pink, Al; red, O; gray, C; white, H) the spin distributions are shown, green indicates β-electron excess, red indicates α-electron excess. See Figure S11 for depictions of the transition structures.

the entrance channel (Figure S14). Consequently, HAT at the terminal oxygen radical anion site is the only possibility for initial C–H bond activation of methane, in contrast to the related systems $ZnAl_2O_4^+$,[6h] where the initial C–H bond activation can also occur at the $[Zn^{2+},O^{2-}]$ site as heterolytic splitting into CH_3^- and H^+, similar to what happens in the oxidative coupling of CH_4 on MgO.[14]

After the first C–H bond activation, the products ^{2}**P2** + CH_2O are formed in the following way. From ^{2}**3** the most stable intermediate ^{2}**4** is formed in which the $^{\bullet}CH_3$ radical has split into a CH_3^+ ion attached to the bridging O^{2-} ion between Al and Ni and an electron that reduces $Ni^{2+}(d^8)$ to $Ni^+(d^9)$:

$$CH_3^{\bullet}[O^{2-}, Ni^{2+}(d^8)] \rightarrow [CH_3^+O^{2-}, Ni^+(d^9)] \quad (5)$$
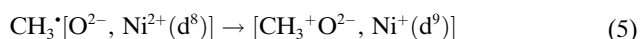
For the change of the Ni oxidation state passing from ^{2}**3** to ^{2}**4**, see Supporting Information Section 4.3 and Table S2. This internal redox process is similar to addition of an H atom to a transition metal oxide species where the proton attaches to the O^{2-} ion and the electron reduces the metal ion (proton coupled electron transfer).[6n, 15]

The next step, ^{2}**4**→^{2}**5**, is hydride transfer from the CH_3O^- species to Ni^+:

$$[CH_3^+O^{2-}, Ni^+(d^9)] \rightarrow [CH_2O, Ni^+(d^9), H^-] \quad (6)$$
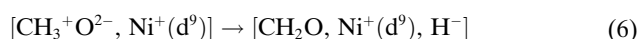
Cleavage of the $Ni–CH_2$ bond then forms the formaldehyde ($H_2C=O$) moiety (^{2}**5**→^{2}**6**). Finally, the intermediate ^{2}**6** rearranges into a more stable structure ^{2}**9**, with the hydride moved from Ni to Al and $CH_2=O$ from Al to Ni (^{2}**6**→^{2}**7**→^{2}**8**→^{2}**9**). Desorption of formaldehyde from inter-

mediate ^{2}**9** requires $174\,kJ\,mol^{-1}$ yielding ^{2}**P2**, which lies well below the energy of the entrance channel ($-147\,kJ\,mol^{-1}$). Modelling of the direct desorption of CH_2O from the Al site in **7** or **8** following a minimum energy pathway resulted in a transfer of the formaldehyde molecule to the Ni atom indicating a much higher barrier for the Al–O bond vs. Ni–O bond cleavage.

We find no evidence that syngas ($CO+H_2$) was generated instead of $H_2C=O$, but also cannot exclude it. DFT predicts that $CO+H_2$ formation starting from intermediate ^{2}**5** (Figure S15) is less favorable by about $21\,kJ\,mol^{-1}$, an energy difference that is within the uncertainty limits of DFT. Moreover, neither the H_2 nor the CO adduct of ^{2}**P2**, which correspond to $NiAl_2O_3H_4^+$ and $NiAl_2O_4CH_2^+$, respectively, were detected mass spectrometrically. However, this is also not conclusive, since mass spectrometric methods typically only detect the product ions and not the neutral product(s), although there are fortitudinous exceptions in which the neutral product molecule remains bound to the product ion.[9]

Although the formation of **P1** is less exothermic than that of **P2**, it is entropically preferred due to release of the $^{\bullet}CH_3$ moiety. At 298 K and an assumed pressure of 1 atm the Gibbs free energy for **P1**, $-107\,kJ\,mol^{-1}$, is lower than that of the highest barrier (^{2}**1**/^{2}**2**) in the pathway for the **P2** generation, $-82\,kJ\,mol^{-1}$, see Supporting Information Section 4.4 Table S3. However, due to the small partial pressures in the present gas-phase experiments, the collision-induced thermalization is slow and, hence, we cannot assume that a transition state is in thermal equilibrium with the corresponding reactants. Instead, we have to consider constant total energy conditions. Therefore, we use RRKM

theory to estimate rate constants for the conversion of $^2\mathbf{1}\rightarrow{}^2\mathbf{1}/{}^2\mathbf{2}$ vs. $^2\mathbf{1}\rightarrow{}^3\mathbf{P1}$ (see Supporting Information Section 4.5 Table S4) which indeed confirm the experimentally observed, favored formation of **P1** (kinetic control).

In summary, the gas-phase reaction of $NiAl_2O_4^+$ with methane has been studied using ion trap mass spectrometry combined with IRPD spectroscopy and DFT. Both the reactant and product ion structures are spectroscopically identified. $NiAl_2O_4^+$ converts methane to formaldehyde, which distinguishes it from many small (transition) metal oxide radical clusters that were previously studied. Before, selective formation of formaldehyde was observed for the reaction of $Al_2O_3^+$ with CH_4.[18] However, the first step for $H_2C{=}O$ formation is different: the terminal radical O atom inserts into the C–H bond of methane yielding methanol and leaving the electron at one of the Al atoms. Other TM-doped alumina clusters like $FeAl_2O_4^+$ and $ZnAl_2O_4^+$ do not produce formaldehyde. Hence the reactivity of $NiAl_2O_4^+$ is attributed to the particular redox properties of the Ni site, especially its stable d-shell configurations and the resulting oxidation states.

Acknowledgements

Conflict of Interest

The authors declare no conflict of interest.

Data Availability Statement

The data that support the findings of this study are available from the corresponding author upon reasonable request.

[1] a) W. Cai, J. Yu, C. Anand, A. Vinu, M. Jaroniec, *Chem. Mater.* **2011**, *23*, 1147–1157; b) L. Xu, H. Song, L. Chou, *ACS Catal.* **2012**, *2*, 1331–1342; c) W. Wu, Z. Wan, W. Chen, M. Zhu, D. Zhang, *Microporous Mesoporous Mater.* **2015**, *217*, 12–20; d) L. Fu, H. Yang, Y. Hu, D. Wu, A. Navrotsky, *Chem. Mater.* **2017**, *29*, 1338–1349; e) I. K. M. Yu, A. Hanif, D. C. W. Tsang, A. C. K. Yip, K. A. Lin, B. Gao, Y. S. Ok, C. S. Poon, J. Shang, *Sci. Total Environ.* **2020**, *704*, 135414; f) E. C. Nykwest, D. Trujillo, S. P. Alpay, *Sci. Rep.* **2021**, *11*, 6410.

[2] a) A. Finiels, F. Fajula, V. Hulea, *Catal. Sci. Technol.* **2014**, *4*, 2412–2426; b) Z. Li, N. M. Schweitzer, A. B. League, V. Bernales, A. W. Peters, A. B. Getsoian, T. C. Wang, J. T. Miller, A. Vjunov, J. L. Fulton, J. A. Lercher, C. J. Cramer, L. Gagliardi, J. T. Hupp, O. K. Farha, *J. Am. Chem. Soc.* **2016**, *138*, 1977–1982; c) J. J. Varghese, S. H. Mushrif, *J. Phys. Chem. C* **2017**, *121*, 17969–17981; d) G. Zhang, C. Yang, J. T. Miller, *ChemCatChem* **2018**, *10*, 961–964.

[3] a) X. Cui, W. Li, P. Ryabchuk, K. Junge, M. Beller, *Nat. Catal.* **2018**, *1*, 385–397; b) M. C. Wasson, C. T. Buru, Z. Chen, T. Islamoglu, O. K. Farha, *Appl. Catal. A* **2019**, *586*, 117214.

[4] a) D. K. Böhme, H. Schwarz, *Angew. Chem. Int. Ed.* **2005**, *44*, 2336–2354; *Angew. Chem.* **2005**, *117*, 2388–2406; b) J. Sauer, H.-J. Freund, *Catal. Lett.* **2015**, *145*, 109–125.

[5] a) S. Feyel, J. Döbler, R. Höckendorf, M. K. Beyer, J. Sauer, H. Schwarz, *Angew. Chem. Int. Ed.* **2008**, *47*, 1946–1950; *Angew. Chem.* **2008**, *120*, 1972–1976; b) X. Rozanska, J. Sauer, *J. Phys. Chem. A* **2009**, *113*, 11586–11594; c) X.-N. Li, X.-P. Zou, S.-G. He, *Chin. J. Catal.* **2017**, *38*, 1515–1527; d) H. Schwarz, P. Gonzalez-Navarrete, J. L. Li, M. Schlangen, X. Y. Sun, T. Weiske, S. D. Zhou, *Organometallics* **2017**, *36*, 8–17; e) H. Schwarz, K. R. Asmis, *Chem. Eur. J.* **2019**, *25*, 2112–2126.

[6] a) Z.-C. Wang, X.-N. Wu, Y.-X. Zhao, J.-B. Ma, X.-L. Ding, S.-G. He, *Chem. Phys. Lett.* **2010**, *489*, 25–29; b) J.-B. Ma, Z.-C. Wang, M. Schlangen, S.-G. He, H. Schwarz, *Angew. Chem. Int. Ed.* **2012**, *51*, 5991–5994; *Angew. Chem.* **2012**, *124*, 6093–6096; c) Y. X. Zhao, Z. Y. Li, Z. Yuan, X. N. Li, S. G. He, *Angew. Chem. Int. Ed.* **2014**, *53*, 9482–9486; *Angew. Chem.* **2014**, *126*, 9636–9640; d) H. Schwarz, *Chem. Phys. Lett.* **2015**, *629*, 91–101; e) Y.-K. Li, Z. Yuan, Y.-X. Zhao, C. Zhao, Q.-Y. Liu, H. Chen, S.-G. He, *J. Am. Chem. Soc.* **2016**, *138*, 12854–12860; f) H. Schwarz, S. Shaik, J. Li, *J. Am. Chem. Soc.* **2017**, *139*, 17201–17212; g) S. D. Zhou, L. Yue, M. Schlangen, H. Schwarz, *Angew. Chem. Int. Ed.* **2017**, *56*, 14297–14300; *Angew. Chem.* **2017**, *129*, 14486–14490; h) X.-H. Zhou, Z.-Y. Li, L.-X. Jiang, S.-G. He, T.-M. Ma, *ChemistrySelect* **2017**, *2*, 991–996; i) S. Debnath, H. Knorke, W. Schöllkopf, S. D. Zhou, K. R. Asmis, H. Schwarz, *Angew. Chem. Int. Ed.* **2018**, *57*, 7448–7452; *Angew. Chem.* **2018**, *130*, 7570–7574; j) Y. K. Li, Y. X. Zhao, S. G. He, *J. Phys. Chem. A* **2018**, *122*, 3950–3955; k) Y. X. Zhao, Z. Y. Li, Y. Yang, S. G. He, *Acc. Chem. Res.* **2018**, *51*, 2603–2610; l) S. D. Zhou, X. Y. Sun, L. Yue, M. Schlangen, H. Schwarz, *Chem. Eur. J.* **2018**, *24*, 14649–14653; m) S. D. Zhou, X. Y. Sun, L. Yue, M. Schlangen, H. Schwarz, *Chem. Eur. J.* **2019**, *25*, 2967–2971; n) F. Müller, J. B. Stuckrath, F. A. Bischoff, L. Gagliardi, J. Sauer, S. Debnath, M. Jorewitz, K. R. Asmis, *J. Am. Chem. Soc.* **2020**, *142*, 18050–18059.

[7] G. Santambrogio, E. Janssens, S. Li, T. Siebert, G. Meijer, K. R. Asmis, J. Doebler, M. Sierka, J. Sauer, *J. Am. Chem. Soc.* **2008**, *130*, 15143–15149.

[8] a) N. M. Reilly, G. E. Johnson, A. W. Castleman in *Model Systems in Catalysis: Single Crystals to Supported Enzyme Mimics* (Ed.: R. Rioux), Springer New York, New York, **2010**, pp. 293–317; b) S. M. Lang, T. M. Bernhardt, *Phys. Chem. Chem. Phys.* **2012**, *14*, 9255–9269; c) H. Schwarz, *Angew. Chem. Int. Ed.* **2015**, *54*, 10090–10100; *Angew. Chem.* **2015**, *127*, 10228–10239.

[9] Y. K. Li, S. Debnath, M. Schlangen, W. Schöllkopf, K. R. Asmis, H. Schwarz, *Angew. Chem. Int. Ed.* **2019**, *58*, 18868–18872; *Angew. Chem.* **2019**, *131*, 19044–19048.

[10] N. Heine, K. R. Asmis, *Int. Rev. Phys. Chem.* **2015**, *34*, 1–34.

[11] a) J. P. Perdew, *Phys. Rev. B* **1986**, *33*, 8822–8824; b) A. D. Becke, *J. Chem. Phys.* **1993**, *98*, 5648–5652.

[12] A. Schäfer, C. Huber, R. Ahlrichs, *J. Chem. Phys.* **1994**, *100*, 5829–5835.

[13] a) L. J. M. Kempkes, J. Martens, G. Berden, K. J. Houthuijs, J. Oomens, *Faraday Discuss.* **2019**, *217*, 434–452; b) Y.-K. Li, M. C. Babin, S. Debnath, T. Iwasa, S. Kumar, T. Taketsugu,

Angew. Chem. Int. Ed. **2022**, *61*, e202202297 (5 of 6)

© 2022 The Authors. Angewandte Chemie International Edition published by Wiley-VCH GmbH

K. R. Asmis, A. Lyalin, D. M. Neumark, *J. Phys. Chem. A* **2021**, *125*, 9527–9535.

[14] K. Kwapien, J. Paier, J. Sauer, M. Geske, U. Zavyalova, R. Horn, P. Schwach, A. Trunschke, R. Schlögl, *Angew. Chem. Int. Ed.* **2014**, *53*, 8774–8778; *Angew. Chem.* **2014**, *126*, 8919–8923.

[15] a) J. Li, S. Zhou, J. Zhang, M. Schlangen, T. Weiske, D. Usharani, S. Shaik, H. Schwarz, *J. Am. Chem. Soc.* **2016**, *138*, 7973–7981; b) T. F. Markle, J. W. Darcy, J. M. Mayer, *Sci. Adv.* **2018**, *4*, eaat5776 ; c) C. A. Gaggioli, J. Sauer, L. Gagliardi, *J. Am. Chem. Soc.* **2019**, *141*, 14603–14611.

[16] I. J. Steinfeld, S. J. Francisco, L. W. Hase, *Chemical Kinetics and Dynamics*, Prentice-Hall, Upper Saddle River, **1999**, pp. 287–383.

[17] T. Beyer, D. F. Swinehart, *Commun. ACM* **1973**, *16*, 379.

[18] Z.-C. Wang, N. Dietl, R. Kretschmer, J.-B. Ma, T. Weiske, M. Schlangen, H. Schwarz, *Angew. Chem. Int. Ed.* **2012**, *51*, 3703–3707; *Angew. Chem.* **2012**, *124*, 3763–3767.